Nuclear Science and Techniques (2025) 36:132
https://doi.org/10.1007/s41365-025-01743-y

Data analysis framework for silicon strip detector in compact spectrometer for heavy-ion experiments

Xiao-Bao Wei[1,2] · Yu-Hao Qin[3] · Sheng Xiao[3] · Da-Wei Si[3] · Dong Guo[3] · Zhi Qin[3] · Fen-Hai Guan[3] · Xin-Yue Diao[3] · Bo-Yuan Zhang[3] · Bai-Ting Tian[3] · Jun-Huai Xu[3] · Tian-Ren Zhuo[1] · Yi-Bo Hao[1] · Zeng-Xiang Wang[1,2] · Shi-Tao Wang[2,4] · Chun-Wang Ma[1,5] · Yi-Jie Wang[3] · Zhi-Gang Xiao[3,6]

Received: 4 March 2025 / Revised: 9 April 2025 / Accepted: 22 April 2025 / Published online: 1 June 2025

Abstract
We developed a dedicated data analysis framework for silicon strip detector telescopes (SSDTs) of the Compact Spectrometer for Heavy-IoN Experiments (CSHINE) that addresses the challenges of processing complex signals. The framework integrates advanced algorithms for precise calibration, accurate particle identification, and efficient event reconstruction, aiming to account for critical experimental factors such as charge-sharing effects, multi-hit event resolution, and detector response nonuniformity. Its robust performance was demonstrated through the successful analysis of light-charged particles in the 25 MeV/u ^{86}Kr + ^{124}Sn experiment conducted at the first Radioactive Ion Beam Line in Lanzhou, allowing for precise extraction of physical observables, including energy, momentum, and particle type. Furthermore, utilizing the reconstructed physical information, such as the number of effective physical events and energy spectra to optimize the track recognition algorithm, the final track recognition efficiencies of approximately 90% were achieved. This framework establishes a valuable reference methodology for SSDT-based detector systems in heavy-ion reaction experiments, thereby significantly enhancing the accuracy and efficiency of data analysis in nuclear physics research.

Keywords CSHINE · Si-Si-CsI telescope · Silicon strip detector · Energy calibration · Particle identification · Track reconstruction · Heavy-ion collisions

1 Introduction

Accurate particle identification (PID) in nuclear reaction experiments spanning intermediate to relativistic energies remains a significant challenge in radioactive ion beam facilities. The complexity of this task has been further exacerbated by the rapid expansion of detector systems, where even state-of-the-art artificial intelligence algorithms exhibit

This work was supported by the National Natural Science Foundation of China (NNSFC) (Nos. 12375123, 12205160, and 12335008), the Natural Science Foundation of Henan Province, China (No. 242300421048), and the postgraduate research and practice innovation project of Henan Normal University (No. YB202402).

✉ Chun-Wang Ma
machunwang@126.com

✉ Yi-Jie Wang
yj-wang15@tsinghua.org.cn

✉ Zhi-Gang Xiao
xiaozg@tsinghua.edu.cn

[1] College of Physics, Centre for Theoretical Physics, Henan Normal University, Xinxiang 453007, China

[2] Institute of Modern Physics, Chinese Academy of Sciences, Lanzhou 730000, China

[3] Department of Physics,Tsinghua University, Beijing 100084, China

[4] School of Nuclear Science and Technology, University of Chinese Academy of Sciences, Beijing 100049, China

[5] Institute of Nuclear Science and Technology, Henan Academy of Sciences, Zhengzhou 450046, China

[6] Center of High Energy Physics, Tsinghua University, Beijing 100084, China

limitations in reliably distinguishing reaction products for fundamental identification tasks [1]. As a series of PID detector systems for light particles (such as p, d, t, etc.), the Compact Spectrometer for Heavy IoN Experiments (CSHINE) system has been constructed to explore the equation of state of nuclear matter near and below the saturation density in the Fermi energy regime [2, 3], which has been installed at the final focal plane of the first Radioactive Ion Beam Line in Lanzhou (RIBLL-I) [4, 5].

The layout of the newly developed CSHINE-III, as illustrated in Fig. 1, integrates three specialized subsystems for comprehensive particle identification: silicon strip detector telescopes (SSDTs) for light-charged particles (LCPs), large area parallel plate avalanche counters (PPACs) for fission fragment (FF) detection, and a CsI(Tl)-based gamma array. SSDTs demonstrate exceptional performance in terms of energy and position resolution, enabling the precise identification of LCPs [6, 7]. This capability has facilitated the discovery of the "ping-pong" emission modality through the isobaric yield ratios of the $A = 3$ nuclei coincident with heavy fragments, and provides critical information on the effects of nuclear symmetry energy on hydrogen emission patterns via the correlation function of the $Z = 1$ isotopes [8–10]. Three large-area PPACs, each with an active detection area of 240 mm × 280 mm, were used for FF measurements and coincidence analysis with LCPs [11]. These measurements have revealed the characteristic features of fast fission processes in heavy-ion reactions, particularly the formation and evolution of low-density, neutron-rich neck structures, which offer valuable constraints on the nuclear symmetry energy compared to transport model simulations [12–14]. The gamma detection system comprises 15 CsI(Tl) crystals (70 mm×70 mm×250 mm each), providing crucial information on the high-momentum tail of nucleon distributions and the nuclear symmetry energy at supra-saturation densities [15, 16]. This integrated detector configuration enables the simultaneous measurement of multiple reaction channels, significantly enhancing the capability of the system to probe nuclear matter properties.

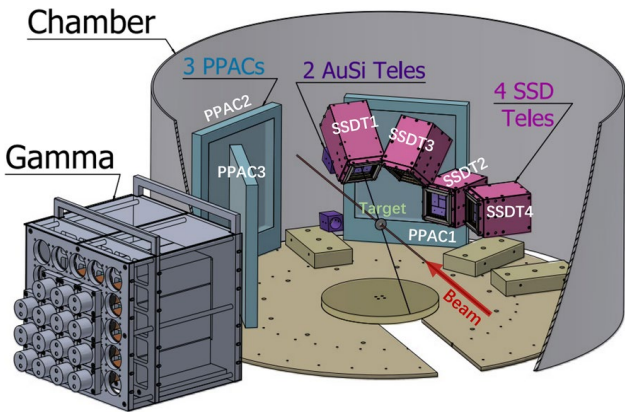

Fig. 1 (Color online) Schematic layout of the CSHINE-III experimental setup, showing the comprehensive detector configuration and relative positioning of its subsystems. Detailed information regarding the individual components is provided in the main text

In the experimental setup, signals generated by incident particles in the detector system are processed through dedicated electronics before being recorded event-by-event by the data acquisition (DAQ) system. Before detailed physical analysis, raw binary data must undergo calibration and reconstruction to accurately represent physical events and transform them into meaningful observables that include multiplicity, particle type, energy, momentum, velocity, and incident angle. The silicon strip telescope, which serves as the core detector in the CSHINE spectrometer, consists of a single-sided silicon strip detector (SSSSD) coupled with a double-sided silicon strip detector (DSSSD), backed by a 3 × 3 CsI(Tl) crystal matrix. The SSDs belong to the BB7 series and feature active areas measuring 63.8 mm × 63.8 mm. Each SSD surface is equipped with 32 strips with a width of 2 mm. Table 1 lists the experimental geometries and thickness parameters for the four SSDTs. This SSD-SSD-CsI configuration enables particle identification over a broad energy range through $\Delta E - E$ correlations between the DSSSD-CsI and SSSSD-DSSSD components. Additional technical details are provided in Ref. [2, 7].

Data processing for SSDTs is significantly complex due to the calibration requirements of numerous independent silicon strip detector channels. Accurate physical analysis requires careful consideration of several factors, including detector dead-layer effects, non-uniformity in thin silicon layers, multi-hit events, charge-sharing phenomena, and nonlinear responses of light-charged particles in CsI(Tl) detectors. Building on the previous two rounds of experimental silicon strip data processing methods, an advanced ROOT-based framework was developed to process data from the CSHINE-SSDTs. This framework was successfully implemented in the analysis of LCPs measured in the 25 MeV/u ^{86}Kr + ^{124}Sn experiment conducted at the RIBLL-I

Table 1 The experimental geometry parameters of the four CSHINE-III SSDTs. L is the distance from the detector to the target, θ_{lab} and ϕ_{lab} are polar angle and azimuthal angle of the detector center in the laboratory frame, respectively. The thickness of SSSSD, DSSSD and CsI(Tl) are listed

SSDT no	1	2	3	4
L (mm)	215.5	275.5	195.5	275.5
θ_{lab} (°)	40	60	70	90
ϕ_{lab} (°)	90	0	50	0
SSSSD (μm)	305	104	70	71
DSSSD (μm)	1008	1010	526	535
CsI(Tl) (mm)	50	50	50	50

station of the Heavy Ion Research Facility in Lanzhou, China, establishing a valuable reference methodology for similar telescope detector systems.

The remainder of this paper is organized as follows. Section 2 describes the architecture of the data analysis framework and its processing workflow. Section 3 presents the analysis methodology and the corresponding results. The performance of CSHINE-SSDTs is discussed in Sect. 4. Finally, a summary is provided in Sect. 5.

2 Data analysis framework

Fig. 2 describes the data processing task for silicon strip detector telescopes, in which three primary stages are involved: (1) data format conversion, (2) quality check, detector calibration, and (3) track reconstruction. The CSHINE-III DAQ and trigger signal processing are described in Ref. [3]. The data processing task starts with the raw data in binary form, which is decoded based on electronic module channels and stored in the ROOT TTree object (TreeData). The second step is to optimize the calibration of each detector, for which mapping between the electronic and corresponding detector logic channels is essential. These two foundational steps are integrated into the DAQ framework.

A preliminary quality-check analysis of the raw detector data is required before performing the calibration analysis. This process involves the generation of a one-dimensional spectrum for each detector channel. By analyzing and observing these individual channel spectra, the functionality of each detector channel can be preliminarily assessed to ensure data accuracy and enhance the efficiency of data analysis. Silicon detectors exhibit a linear energy response to charged particles and energy deposition is independent of particle type, particularly for light particles [17]. A combined calibration method utilizing a precise pulse generator and α-particle sources was employed. CsI(Tl) scintillators were used as residual energy detectors because of their relatively high stopping power, geometric shape flexibility, minimal radiation damage, cost-effectiveness and good resolution [18]. However, the light output of a scintillator is non-linear and is influenced by both the energy deposited in the crystal and the atomic and mass numbers of the incident ions. Therefore, mass and charge identification must be performed prior to energy calibration. By combining the nominal thickness of the DSSSD provided by the manufacturer and the measured ΔE_2 (MeV), the total residual energy E (MeV) in CsI(Tl) can be calculated for all tracks using the LISE++ toolkit [19]. This calculation process allowed the establishment of a relationship between the ADC channel number and the energy deposition (MeV) in CsI(Tl).

The configuration of the CSHINE SSDT from top to bottom comprises four layers containing hit information:

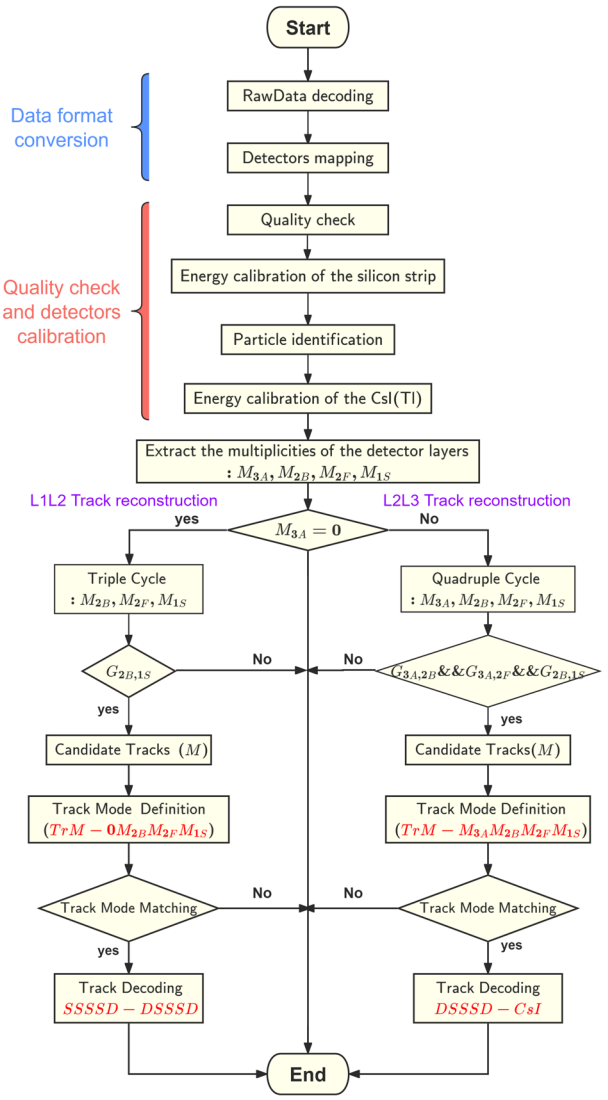

Fig. 2 (Color online) Flow charts of the data processing task for the silicon strip detector telescopes

the SSSSD ("1S"), the DSSSD with front ("2F") and back ("2B") side strips, and the 3×3 CsI(Tl) hodoscope ("3A"). When only a single particle strikes the telescope and is deposited in the hodoscope, the multiplicity of each layer is equal to one, and such events are straightforward to identify. Nevertheless, in the case of simultaneous incidence of multiple particles, the task of discerning all actual tracks becomes more complicated owing to charge-sharing and multi-hit effects. For each event, the multiplicities of all detector layers, M_{3A}, M_{2B}, M_{2F}, and M_{1S}, were extracted. These multiplicities correspond to the number of channels in each layer, where the signal amplitude exceeds a predetermined threshold empirically set above the pedestal for each individual channel. Based on whether the events had particles stopping in the CsI(Tl) hodoscope, the track reconstruction

was divided into two categories: L1L2 (SSSSD-DSSSD) and L2L3 (DSSSD-CsI).

As recently reported in Refs. [6] and [20], the geometric and temporal constraints can be utilized to define the spatial alignment of the tracks and to match the hit times of the detectors. This approach helps eliminate spurious tracks and determine the number of candidate tracks (M). However, despite recording time information on both sides of the DSSSD strips in our experiment, the high time threshold set for the back-DSSSD resulted in substantial data loss when the time signals of the corresponding front- and back- DSSSD were consistent. Consequently, instead of using time constraints, we relied solely on geometric constraints to determine the candidate tracks. Track modes were defined on the basis of the number of candidate tracks and hit multiplicities in the telescope layers. In L2L3 track reconstruction, the track modes are denoted as "$TrM - M_{3A}M_{2B}M_{2F}M_{1S}$". By contrast, in the L1L2 track reconstruction, they are denoted as "$TrM - 0M_{2B}M_{2F}M_{1S}$". There are a total of M^4 and M^3 different track modes, respectively. However, the analysis revealed that the number of effective modes was much less than the total number of modes. In track decoding, the highest-probability modes are selected, as listed in the appendix Tables 8 and 9, respectively. By incorporating the energy constraints, the issues of charge sharing and multi-hit effects can be effectively addressed. Finally, the events that contain the final physical information are stored.

The silicon strip telescope requires an efficient data processing architecture as the core detector system of the CSHINE spectrometer. To satisfy this requirement, we implemented a modular computational structure in which each distinct processing step was encapsulated within an individual C++ class. These specialized classes were integrated into a comprehensive and unified analysis framework [21]. The functional characteristics of the principal C++ classes within this framework are systematically presented in Table 2.

3 Analysis approach and results

3.1 Detector calibration

3.1.1 Energy calibration of the silicon strip detectors

Strip-by-strip energy calibration is required for SSDs because of their fabrication limitations and the nonuniformity of the associated electronics. Due to the linear energy response of SSDs, the combination of the α source and pulser calibration method was used. Each telescope was equipped with an aluminum Mylar foil entrance window (2.0 μm Mylar + 0.06 μm Al) to protect the detector and provide electromagnetic shielding. For source calibration, a three-component α source comprising ^{239}Pu, ^{241}Am and ^{244}Cm with energies of 5.147, 5.480, and 5.795 MeV, respectively, was used. The energy deposited in the silicon strip detector was corrected according to LISE++ calculations, resulting in calibrated values of 4.904 MeV for ^{239}Pu, 5.248 MeV for ^{241}Am, and 5.571 MeV for ^{244}Cm. An interactive program was developed to fit the peak of the ADC channel (α) and to determine its relationship with $E(\alpha)$, as shown in Fig. 3.

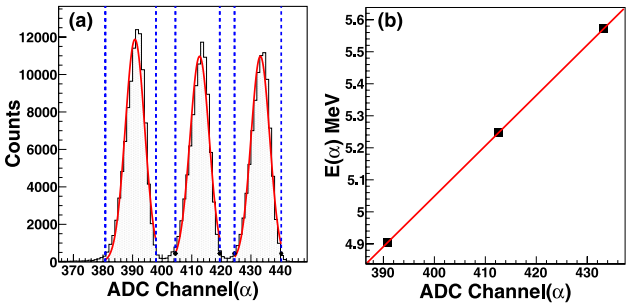

Fig. 3 (Color online) Example energy spectrum of α particles fitting process (left panel) and results checking (right panel) from an individual strip on the single-sided silicon detector at SSDT1

Table 2 The primary C++ classes and main functions in the data analysis framework of CSHINE-SSDTs

Class name	Main function
CSHINEQualityCheck	Quality inspection of experimental data
CSHINEPedestals	Extract the pedestal in the energy spectrum
CSHINEPulserCali	Silicon strip pulse scale
CSHINEAlphaCali	Silicon strip α energy fitting
CSHINESiEnergyCali	Energy calibration of the silicon strip
CSHINECsIEnergyCali	Energy calibration of the CsI(Tl)
CSHINETrackReconstruction	Track Reconstruction
CSHINESiPixelGeometry	Coordinate system transformation
CSHINEEvent	Physical event definition
CSHINEUnCaliDataToPhysicsEvent	Generate final physical data from raw data

Pulser calibration was used to ascertain the response characteristics of the electronics. An automatic peak-finding program was developed to obtain peak values, as shown in Fig. 4a. Linear fitting [Eq. (1)] of the standardized pulse amplitudes (V) and the ADC channel (Ch) was carried out, as shown in 4b.

$$V = k' \times Ch + b' \tag{1}$$

Assuming a linear relationship between V and the energy deposition (ε) through $V = \beta\varepsilon$, the energy calibration was finalized, as shown in Eq. (2):

$$\varepsilon = \frac{k'}{\beta} \times Ch + \frac{b'}{\beta} \tag{2}$$

3.1.2 Particle identification

Particle identification is not only essential to calibrate the CsI(Tl) energy response to different types of incident particles, but also plays a crucial role for hits matching in the track reconstruction process. In the scatter plot $\Delta E - E$, particles with different charges and masses tend to gather in different bands. Typically, PID is performed through graphical cuts around each band. Despite its versatility and ability to accommodate diverse scenarios, this approach suffers from two major limitations. First, in regions characterized by low particle statistics, it fails to extrapolate reliable identification, as there is insufficient data to establish clear cut boundaries. Second, manual contouring of each particle deposited in every Si-CsI(Tl) detection cell is a time-consuming and tedious process. As the number of detection cells increases, the time-consuming problem becomes more pronounced [22]. To address the aforementioned issues, Tassan-Got and Gawlikowicz et al. [23, 24] proposed a novel identification function based on the Bethe-Bloch formula [23, 24]. This function enables accurate modeling of the data and safe extrapolations in data-sparse regions by fitting the ridge lines of each isotope using 14 parameters, as shown in Eq. (3).

$$\begin{aligned}
\Delta E =& [(p_1 E)^{p_2+p_3+1} + (p_4 Z^{p_5} A^{p_6})^{p_2+p_3+1} \\
&+ p_7 Z^2 A^{p_2} (p_1 E)^{p_3}]^{\frac{1}{p_2+p_3+1}} - p_1 E \qquad (a) \\
E =& p_8 W(Z) L + p_9 Z\sqrt{A}\ln(1 + p_{10} W(Z) L) \qquad (b) \\
W(Z) =& p_{11} \frac{\ln(1+p_{12}Z)}{Z}(1 - \exp(-p_{13} Z^{p_{14}})) \qquad (c)
\end{aligned} \tag{3}$$

Here, L is the light output of particles in CsI(Tl) (equivalent to the ADC channel) and $W(Z)$ is a gain factor.

Figure 5a displays the $\Delta E - E$ scattering distribution for one hit events, in which the energy loss ΔE is from the front strips of the DSSSD transmission detector (layer 2) and the energy E is deposited in one CsI(Tl) unit of SSDT1. The sampling points on the isotopes' ridge curves were manually selected and indicated by the red dotted lines. The best fit was achieved with an individual set of parameters constrained by the simultaneous fitting of all visible isotopes. The mass and charge of each particle with given values of ΔE and E can be extracted by inverting the multiparametric identification function. When the extracted mass was not zero, the events were shown in Fig. 5b. As defined in Ref. [23], the particle identification variable PID_n is calculated as $\mathrm{PID}_n = Z_n + 0.2(A_n - 2Z_n)$, where n represents different particles. Figure 5c presents the PID_n spectrum. By fitting the ^{4}He peak to a Gaussian function, the relative mass resolution for the α particle can be derived.

The correction of non-uniformity in the thickness of thin SSDs is of crucial importance for PID. Before correction, the isotopic resolution of the SSSSD-DSSSD component in SSDT2 was comparatively poor, as shown in Fig. 6a. This is due to the random energy deposition when the particles pass through the detector at different positions with varying path lengths. For thickness correction, the sensitive area was divided into 8×8 bins. In each bin, we plotted the $\Delta E_1 - E_2$ histogram individually and selected a specific bin showing clear PID bands as a reference. Subsequently, for the remaining bins, the thickness correction factor η for the SSSSD was adjusted from -0.05 to 0.10 with a step size of 0.005 and the energy loss ΔE_1 in the SSSSD was corrected to $\Delta E_1(1+\eta)$. For each value η, a two-dimensional histogram was generated and compared with the reference histogram. Subsequently, the thickness correction for each bin was determined according to the value η, which provided the best consistency

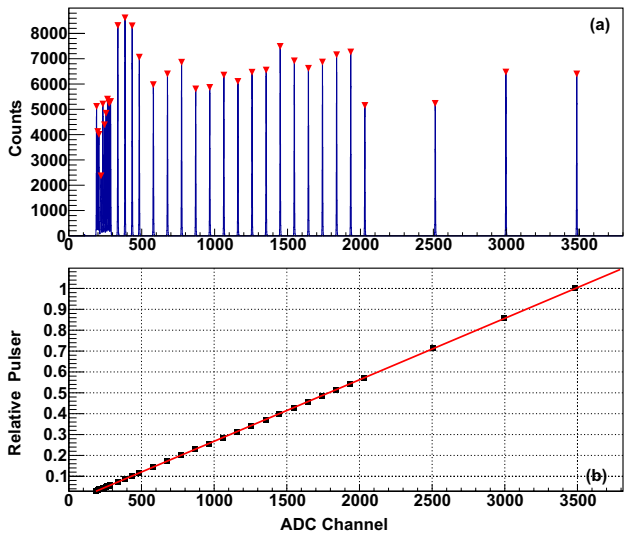

Fig. 4 (Color online) Pulser calibration results for peak-finding (**a**) and linear response fitting (**b**)

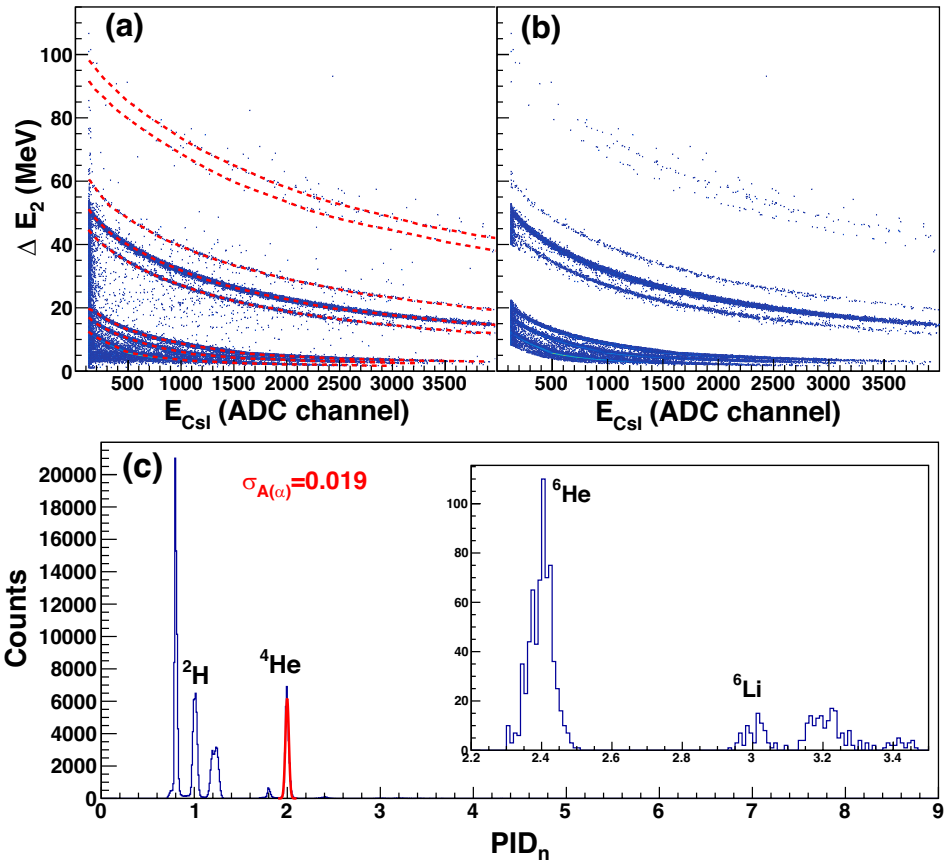

Fig. 5 (Color online) Selected events with only one particle hitting in the DSSSD transmission detector (layer 2) and one CsI(Tl) unit of the SSDT1. Panel **a** shows the $\Delta E_2 - E_{\mathrm{CsI}}$ scattering plot and the manually sampling points on the ridge curves (the dotted red line). Panel **b** displays the results when the extracted mass from inverting the 14-parameter identification function is not zero. Panel **c** is the $\mathrm{PID_n}$ spectrum

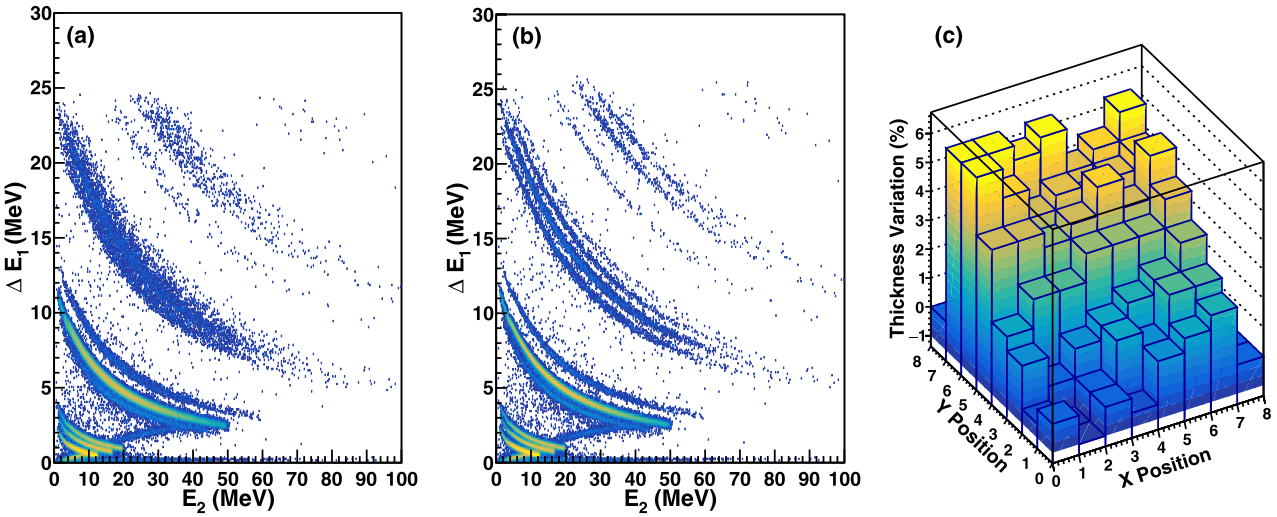

Fig. 6 (Color online) Panel **a** represents a $\Delta E_1 - E_2$ scattering plot of SSDT2 before thickness correction for the 104 μm ΔE_1 SSSSD (the thickness of E_2 detector is 1010 μm). Panel **b** illustrates the two dimensional plot after the thickness correction for the ΔE_1 detector. Panel **c** displays the "relative" thickness correction for the ΔE_1 detector

with the reference histogram. Figure 6b shows the two-dimensional graph after thickness correction for the 104 μm SSSSD, demonstrating a significant improvement in identification resolution compared to the graph before correction in Fig. 6a. Figure 6c illustrates the "relative thickness variation" for the 104 μm SSSSD, ranging from −1% to 7.5%. This approach offers a relative correction for the thickness of a thin ΔE detector with respect to the

reference bin. The absolute thickness correction relies on in-beam tests, as described in Refs. [25, 26].

After thickness correction of the SSSSD, each isotope can be effectively separated. Due to the impact of punching through on the scattering plot $\Delta E_1 - E_2$, the traditional method was used instead of the multiparametric formula. In Fig. 7a, the distinct particles are identified by the green inclusive contour. Additionally, the center of each isotope ridge was fitted by a polynomial,

$$f_n(E) = a_n^0 \cdot E^{-1} + a_n^1 \cdot E^0 + a_n^2 \cdot E^1 + a_n^3 \cdot E^2 + a_n^4 \cdot E^3 + a_n^5 \cdot E^4 + a_n^6 \cdot E^5 + a_n^7 \cdot E^6 \quad (4)$$

where E is the energy deposited in the front strips of the DSSSD detector, a_n^0 to a_n^7 are eight parameters, and n represents the different particles as previously defined. The PID$(E_2, \Delta E_1)$ of each particle can be calculated using Eq. (5). Figure 7b and c display the results after identifying the particles. Table 3 summarizes the relative mass resolution of α particles for each telescope used in the experiment.

Table 3 The relative mass resolution of α particles measured by each telescope

	Relative mass resolution	
Detector	SSSSD-DSSSD	DSSSD-CsI
SSDT1	0.019	0.021
SSDT2	0.026	0.016
SSDT3	0.034	0.024
SSDT4	0.024	0.022

$$\mathrm{PID}(E_2, \Delta E_1) = \mathrm{PID}_n + \frac{\Delta E_1 - f_n(E_2)}{f_{n+1}(E_2) - f_n(E_2)} \cdot (\mathrm{PID}_{n+1} - \mathrm{PID}_n) \quad (5)$$

3.1.3 Energy calibration of the CsI(Tl) crystals

Leveraging the high-quality calibrations of the DSSSD and the multiparametric formula obtained in the PID, the energy loss method can be utilized to perform the energy calibration on the CsI(Tl) crystal. Based on the two-dimensional

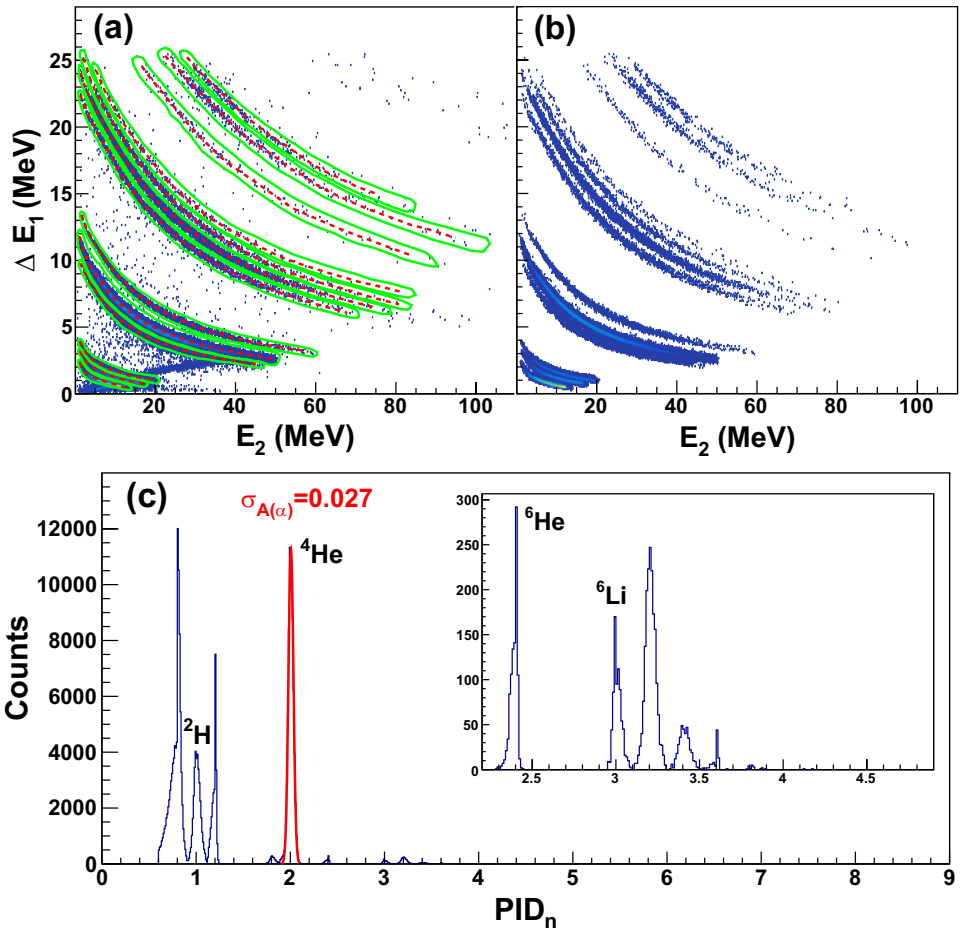

Fig. 7 (Color online) Particle identification of SSDT2 using the traditional method. In panel **a**, distinct particles are identified by the green inclusive contour, and each isotope ridge is marked by a red dotted line. Panel **b** displays the results of events in the graphical cuts. Panel **c** shows the PID$_n$ spectrum

plot for $\Delta E_2 - E_{\mathrm{CsI}}^{\mathrm{ch}}$, the range of $E_{\mathrm{CsI}}^{\mathrm{ch}}$ for each isotope was manually selected. For example, in Fig. 5a, the range for protons is $90 \leq E_{\mathrm{CsI}}^{\mathrm{ch}} \leq 3200$. Next, we selected 30 independent $E_{\mathrm{CsI}}^{\mathrm{ch}}$ points uniformly within this range. Using the multiparametric formula, we determine the corresponding energy loss (ΔE_2) in the DSSSD. Subsequently, the total kinetic energy of the incident particle E_k was deduced by numerically inverting Ziegler's energy loss table [27] based on ΔE_2 and the thickness of the DSSSD. Finally, the energy impinging on the CsI(Tl) crystal ($E_{\mathrm{CsI}}^{\mathrm{MeV}}$) was calculated by subtracting the energy losses in the SSD and Mylar foil that wraps the entrance face of the CsI(Tl) crystal, $E_{\mathrm{CsI}}^{\mathrm{MeV}} = E_k - \Delta E_2 - \Delta E_{\mathrm{Mylar}}$, which corresponds to the energy associated with the initial raw ADC channel $E_{\mathrm{CsI}}^{\mathrm{ch}}$.

Figure 8 shows the results of the energy calibration of the CsI(Tl) crystals for each isotope. The CsI(Tl) energy response for the incident particle exhibited insignificant non-linearity and a slight difference between the isotopes in the energy range of 0 to 100 MeV, in accordance with the results in Ref. [28]. Two separate formulas were used to describe the calibration process. For $Z = 1$ isotopes, the calibration function was written as [28]

$$L(E, Z = 1, A) = a_0 + a_1 E^{(a_2+A)/(a_3+A)} \tag{6}$$

where a_0 is an offset, a_1 is a gain factor, A is the mass number of $Z = 1$ isotope, and a_2, a_3 are empirical non-linearity parameters. The fitting results are presented in Fig. 8a, where three solid lines are depicted: the red line represents the proton, green line represents the deuteron, and purple line represents the triton. For isotopes with $Z \geq 2$, the standard Horn's formula was used for calibration [29],

$$L(E, Z \geq 2, A) = a_0 + a_1 \left(E - a_2 A Z^2 \ln \left| \frac{E + a_2 A Z^2}{a_2 A Z^2} \right| \right) \tag{7}$$

where a_0, a_1 and a_2 are the parameters obtained from the simultaneous fitting of all heavy isotopes. The perfect fitting results are shown in Fig. 8b.

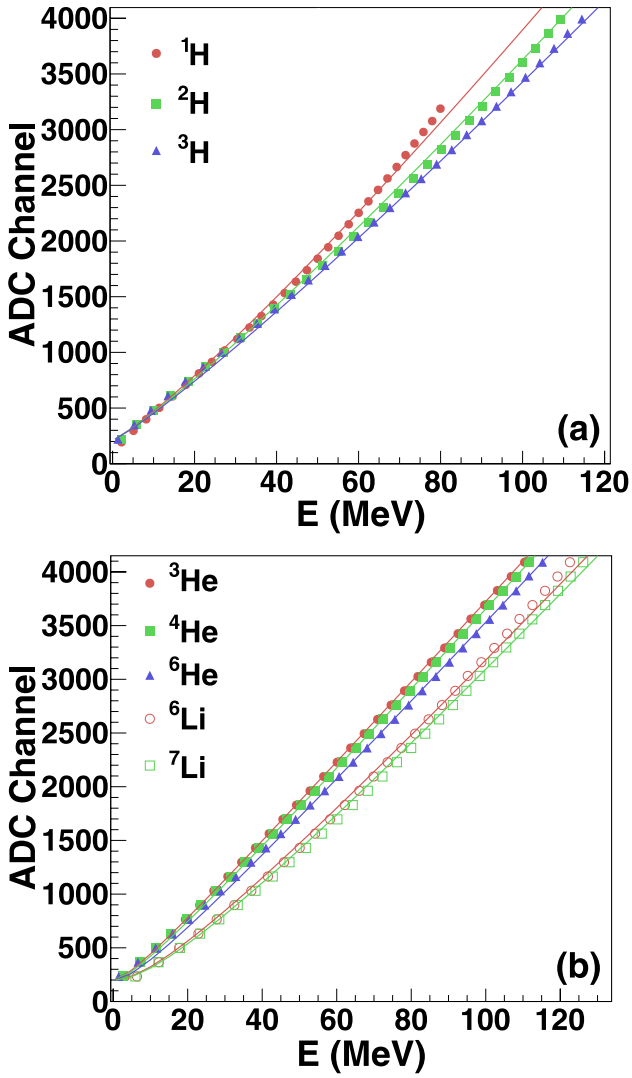

Fig. 8 (Color online) Energy calibration of one CsI(Tl) unit in SSDT1. Panel **a** shows the results for hydrogen isotopes: proton (red points), deuteron (green squares), and triton (purple triangles). The corresponding curves represent the fitting results with Eq. (6). Panel **b** displays the calibration result for heavy ions ^{3,4,6}He, and ^{6,7}Li. The corresponding curves represent the fitting results with Eq. (7)

3.2 Track reconstruction

3.2.1 Constraints analysis

The geometric relationships between different layers are determined solely by the structure of the SSDTs, which is related to the design and installation of the detectors. A valid track with hits in each detector layer should approximately be a straight line. Table 4 provides a detailed geometric mapping of the CSHINE SSDT. For particles that are stopped in a specific unit of the CsI(Tl) crystal, denoted by $N_{3\mathrm{A}}$, only certain strips of DSSSD, marked by $N_{2\mathrm{F}}$ and $N_{2\mathrm{B}}$ for the front and back strips, respectively, satisfy the geometric relationships $G_{3\mathrm{A},2\mathrm{B}}$ and $G_{3\mathrm{A},2\mathrm{F}}$. The incident event of one particle can be used to confirm geometric relationships, as illustrated in Fig. 9. On the surface of each SSD, there were 32 strips with a width of 2 mm, and the gap between adjacent strips was 100 µm. As in the previous experiment, to save electronic channels, every two strips are merged into one channel, and thus, there is a total number of 16 channels on each side. However, an improved merging technique was implemented, where two strips near the edge (first and thirty-second strips) were merged into one channel to minimize the shadow effect in the edge channels. Furthermore, geometric matching between SSSSD strips and DSSSD back strips requires $G_{2\mathrm{B},1\mathrm{S}}$. According to the configuration

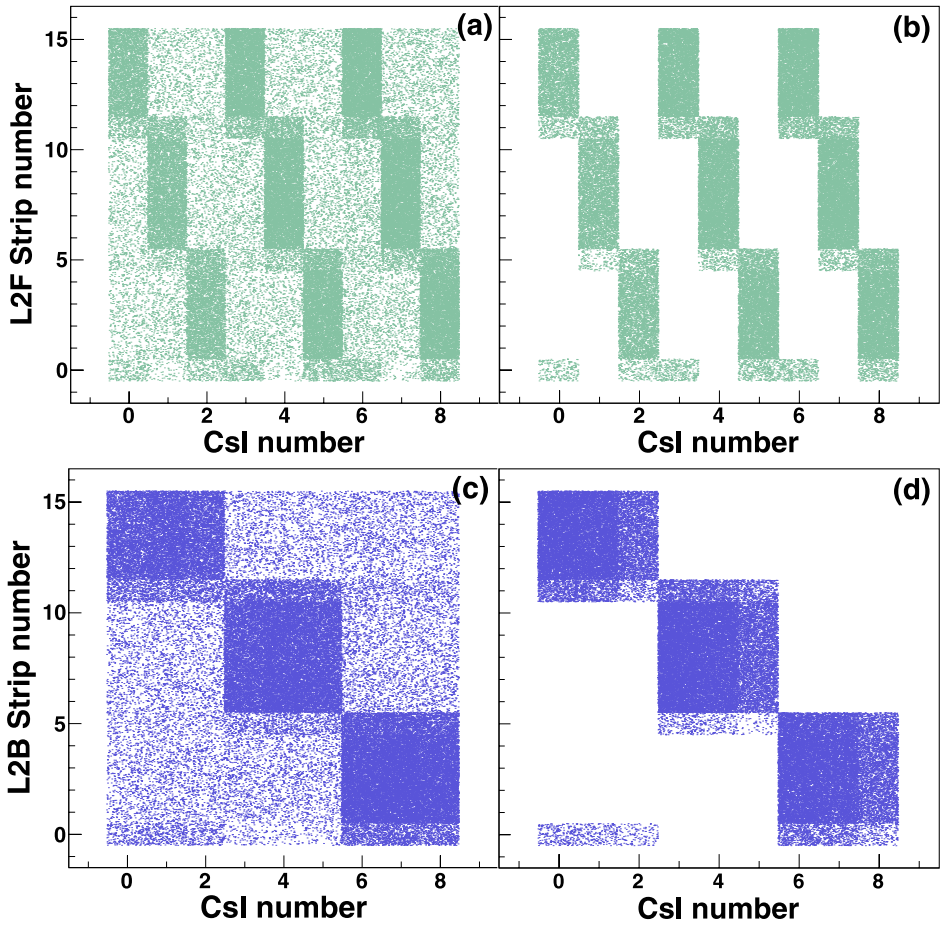

Fig. 9 (Color online) Panels **a** and **c** display scattering plots before applying geometric constraints for one particle incident events in SSDT2, showing the geometric relationship between the front and back sides of the L2 DSSSD and L3 layer CsI(Tl) crystals. Panels **b** and **d** display scattering plots after applying geometric constraints

Table 4 Geometric map of the CSHINE SSDTs. In each telescope, there are 16 channels on each silicon layer and 3×3 CsI(Tl) crystals for the array

SSDT no (N_{Tel})	CsI No ($N_{3\mathrm{A}}$)	"2B" Strip No ($N_{2\mathrm{B}}$)	"2F" Strip No ($N_{2\mathrm{F}}$)	"1S" Strip No ($N_{1\mathrm{S}}$)
1-3	0	$11 \le N_{2\mathrm{B}} \le 15\&0$	$11 \le N_{2\mathrm{F}} \le 15\&0$	
1-3	1	$11 \le N_{2\mathrm{B}} \le 15\&0$	$5 \le N_{2\mathrm{F}} \le 11$	
1-3	2	$11 \le N_{2\mathrm{B}} \le 15\&0$	$0 \le N_{2\mathrm{F}} \le 5$	
1-3	3	$5 \le N_{2\mathrm{B}} \le 11$	$11 \le N_{2\mathrm{F}} \le 15\&0$	
1-3	4	$5 \le N_{2\mathrm{B}} \le 11$	$5 \le N_{2\mathrm{F}} \le 11$	$\lvert N_{2\mathrm{B}} - N_{1\mathrm{S}} \rvert \le 1$
1-3	5	$5 \le N_{2\mathrm{B}} \le 11$	$0 \le N_{2\mathrm{F}} \le 5$	
1-3	6	$0 \le N_{2\mathrm{B}} \le 5$	$11 \le N_{2\mathrm{F}} \le 15\&0$	
1-3	7	$0 \le N_{2\mathrm{B}} \le 5$	$5 \le N_{2\mathrm{F}} \le 11$	
1-3	8	$0 \le N_{2\mathrm{B}} \le 5$	$0 \le N_{2\mathrm{F}} \le 5$	
4	0	$11 \le N_{2\mathrm{B}} \le 15\&0$	$0 \le N_{2\mathrm{F}} \le 5$	
4	1	$11 \le N_{2\mathrm{B}} \le 15\&0$	$5 \le N_{2\mathrm{F}} \le 11$	
4	2	$11 \le N_{2\mathrm{B}} \le 15\&0$	$11 \le N_{2\mathrm{F}} \le 15\&0$	
4	3	$5 \le N_{2\mathrm{B}} \le 11$	$0 \le N_{2\mathrm{F}} \le 5$	
4	4	$5 \le N_{2\mathrm{B}} \le 11$	$5 \le N_{2\mathrm{F}} \le 11$	$\lvert N_{2B} - N_{1S} \rvert \le 1$
4	5	$5 \le N_{2\mathrm{B}} \le 11$	$11 \le N_{2\mathrm{F}} \le 15\&0$	
4	6	$0 \le N_{2\mathrm{B}} \le 5$	$0 \le N_{2\mathrm{F}} \le 5$	
4	7	$0 \le N_{2\mathrm{B}} \le 5$	$5 \le N_{2\mathrm{F}} \le 11$	
4	8	$0 \le N_{2\mathrm{B}} \le 5$	$11 \le N_{2\mathrm{F}} \le 15\&0$	
DSSSD-CsI		$G_{3\mathrm{A},2\mathrm{B}}$	$G_{3\mathrm{A},2\mathrm{F}}$	$G_{2\mathrm{B},1\mathrm{S}}$
SSSSD-DSSSD				$G_{2\mathrm{B},1\mathrm{S}}$

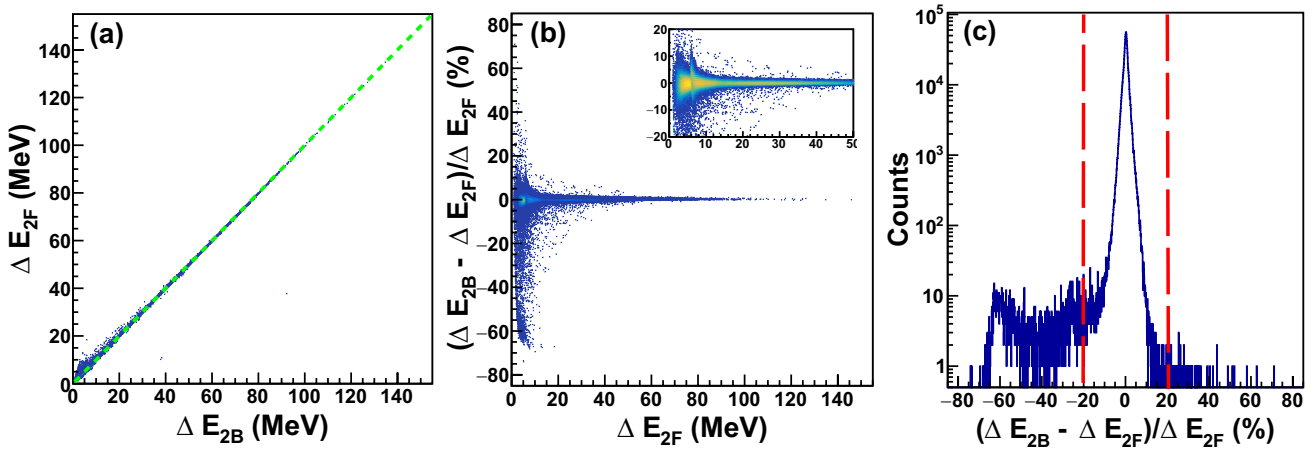

Fig. 10 (Color online) **a** The correlation between the energies detected in the front- (ΔE_{2F}) and back-sides (ΔE_{2B}) of the DSSSD in SSDT1. **b** The relative difference between ΔE_{2F} and ΔE_{2B} as a function of ΔE_{2F}. **c** The spectrum of relative differences in a logarithmic scale

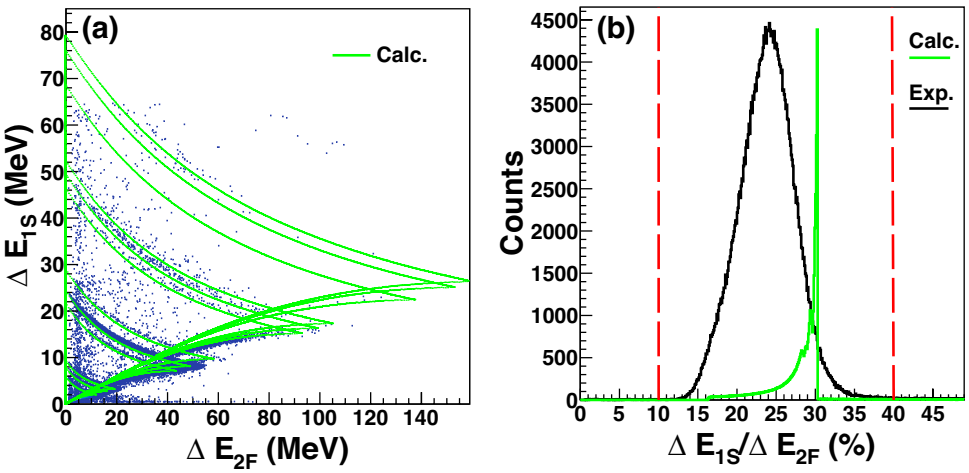

Fig. 11 (Color online) Panel **a** displays the experimental scattering plot of $\Delta E_{1S} - \Delta E_{2F}$ compared with the calculations using LISE++. In panel **b**, the distributions of $\Delta E_1/\Delta E_2$ are presented. The black curve denotes the experimental result, while the green curve represents the calculated result

Table 5 Energy constraints of the CSHINE SSDT1. The thickness of the SSSSD and DSSSD are 305 μm and 1008 μm, respectively

Cases	Constrains	Descriptions
DSSSD-CsI	$E^{iso}_{3A,2F}$	The extracted mass is not zero
	$E_{2F,1S}$	$0.10 \le \Delta E_{1S}/\Delta E_{2F} \le 0.40$
SSSSD-DSSSD	$E_{2B,2F}$	$\lvert(\Delta E_{2B} - \Delta E_{2F})/\Delta E_{2F}\rvert \le 0.20$
	$E^{iso}_{2F,1S}$	$(E_{2F}, \Delta E_{1S})$ inside an isotope cut

of the CSHINE SSDT, the SSSSD and the back strips of the DSSSD are in parallel and numbered in the same direction. Because the distance between the SSDs is relatively shorter compared to the distance from the target, hits of a single track on the SSSSD and the backside of the DSSSD will occur on the same or neighboring strip numbers, as restricted by $G_{2B,1S}$ of $|N_{2B} - N_{1S}| \le 1$.

Table 5 lists the energy constraints that should be met for the particles stopped in DSSSD or CsI(Tl). During the particle identification process, the relationship between ΔE and E was determined. For DSSSD-CsI, the multiparametric identification function can be used to determine the mass of a particle using the information of the deposited energies ($E_{3A}, \Delta E_{2F}$). The extracted mass should not be zero, denoted as $E^{iso}_{3A,2F}$. For SSSSD-DSSSD, the deposited energies of the particle ($E_{2F}, \Delta E_{1S}$) should fall into the banana-shaped graphical cut corresponding to a specific isotope, which is represented by $E^{iso}_{2F,1S}$. Another important constraint is the relationship between the energies detected on the front (ΔE_{2F}) and back sides (ΔE_{2B}) of the DSSSD, indicated by $E_{2B,2F}$, and utilized for both the DSSSD-CsI and SSSSD-DSSSD cases. Figure 10 presents a processing example demonstrating how to determine the constraints of $E_{2B,2F}$ for SSDT1. Events of single particle incidence, where the particle stops at CsI(Tl) and is constrained by

three geometric constraints, were selected to investigate the relationship between ΔE_{2F} and ΔE_{2B}. This selection was performed to avoid the influence of inter-strip events. Figure 10a shows that ΔE_{2F} and ΔE_{2B} are approximately equal. To improve the precision of the constraint, the relative difference $(\Delta E_{2B} - \Delta E_{2F})/\Delta E_{2F}$ is defined and its absolute value should be less than 0.2, as shown in Fig. 10c. Finally, events that stop at CsI(Tl) can be constrained by the energy loss ratio $\Delta E_1/\Delta E_2$ between the two silicon detectors. Based on the thicknesses of the SSDs, the energy loss of the particles as they penetrate the two SSDs was calculated using LISE++. The comparison between the calculated values and the experimental results is shown in Fig. 11. The left panel is a scattering plot of $\Delta E_{1S} - \Delta E_{2F}$, which confirms the reliability of the calculated values. The right panel displays the distributions of $\Delta E_1/\Delta E_2$, where the black and green curves represent the experimental and calculated results, respectively. In this study, only the calculated and experimental distribution ranges of $\Delta E_1/\Delta E_2$ were utilized as an additional criterion for track recognition. However, the difference in shape between the calculated and experimental spectra, which stems from the simplified assumption of a uniform incident energy distribution used in the simulations, was not taken into account. Taking SSDT1 as an example, the energy constraint $E_{2F,1S}$ was determined as $0.10 \leq \Delta E_{1S}/\Delta E_{2F} \leq 0.40$.

3.2.2 Track decoding

Two types of track decoding start from DSSSD and CsI(Tl), respectively. By considering the multiplicities extracted from each detector layer and matching them in a loop, all the possible cases can be comprehensively covered. Screening out candidate tracks through geometric constraint is crucial, as this process can eliminate a significant number of false tracks.

Table 6 lists some typical track modes that display charge-sharing and multi-hit effects, providing the basic characteristics for decoding complex track modes. In the track decoding algorithm, it is reasonable to assume that charge sharing only occurs between two adjacent channels in the same layer, denoted by $G_{O}^{\text{sharing}_{ij}}$, where i and j are the candidate track numbers and the subscript O represents the layer. In the cases of SSSSD-DSSSD, we exemplify the charge-sharing effect by taking one Tr2-211 event. The sum of the energy losses in the two adjacent strips, strip 11 and strip 12, in the "2B" layer has been shown to be approximately equal to the energy loss in the single strip 11 on the "2F" layer. This result meets the energy constraint $E_{2B_{sum_{12}},2F}$. If $E^{iso}_{2F_1,1S_1}$ is also true, then one real track is finally determined. The track decoding flow diagram for this mode is shown in Fig. 12a. In Table 6, Tr2-212 represents an event in which two valid candidate tracks exist. In this event, the two particles strike the same strip on the "2F" layer. In such cases, E_{2B} is used instead of E_{2F} for particle identification when double hits occur on the front side of the DSSSD. Both tracks must satisfy the energy constraint $E^{iso}_{2F_i,1S_i}$ simultaneously, denoted as $E^{\text{iso-2Hit}_{12}}_{2B_{scale_{12}},1S_{12}}$. Figure 12b shows the complete decoding process of Tr2-212, which also needs to be checked for the inter-strip effect if the multi-hit energy constraint mentioned above is not satisfied.

In the DSSSD-CsI case, considering track mode Tr2-1121[a] as an example, which includes the inter-strip effect that occurs in the "2F" layer, the sum of the energy losses in the two neighboring strips 12 and 13 in the "2F" layer and the energy deposited in the crystal should satisfy the energy constraint $E^{iso}_{3A_1,2F_{sum_{1,2}}}$. In addition, two constraints, $G_{2F}^{\text{sharing}_{12}}$ and $E_{2B_1,2F_{sum_{12}}}$, were applied to guarantee the correct determination of the energy of the inter-strip event. Moreover, to complete the reconstruction of the track, we must cross-check the energy loss ΔE_{1S} in the "1S" layer. This is achieved using the energy constraint $E_{2F,1S}$. If this constraint is not satisfied, ΔE_{1S} can be recalculated by the following procedures: (1) the charge (Z) and mass (A) of the particle can be obtained from $E^{iso}_{3A_1,2F_{sum_{1,2}}}$; (2) the energy of the particle impinging the DSSSD, E_2^{imp}, can be deduced by the LISE++; (3) the energy of the particle impinging the SSSSD, E_1^{imp}, can also be deduced similarly; (4) the particle's energy loss in the SSSSD is finally obtained with E_2^{imp}-E_1^{imp}. Figure 13a shows the flow diagram of the Tr2-1121 track mode.

wTrack recognition efficiency is defined as the ratio of the number of successful track recognition events to the number of candidate events that meet the geometric constraints. In this study, we introduced reconstruction information, such as the final effective identification event number and energy spectra, into the track recognition algorithm to optimize the detector signal threshold. With this improvement, track recognition efficiency was further enhanced compared to our previous work [6]. As shown in Table 7, the track recognition efficiencies of all telescopes approached 90% in this experiment.

4 Performance of CSHINE-SSDTs

The characteristic correlation peaks observed in the relative momentum distributions of a pair of particles serve as vital indicators to evaluate the calibration and performance of the detector [30]. As shown in Fig. 14, the

Table 6 Data characteristics of some typical track modes

SSSSD-DSSSD charge sharing: Tr2-211								
Track no	N_{3A}	N_{2B}	N_{2F}	N_{1S}	E_{3A} (ch)	ΔE_{2B} (MeV)	ΔE_{2F} (MeV)	ΔE_{1S} (MeV)
1	-	**11**	4	11	-	**6.2**	9.3	1.2
2	-	**12**	4	11	-	**3.0**	9.3	1.2
SSSSD-DSSSD Multi-hit: Tr2-212								
Track no	N_{3A}	N_{2B}	N_{2F}	N_{1S}	E_{3A} (ch)	ΔE_{2B} (MeV)	ΔE_{2F} (MeV)	ΔE_{1S} (MeV)
1	-	**1**	4	**1**	-	**50.9**	64.1	**28.4**
2	-	**6**	4	**6**	-	**13.5**	64.1	**1.9**
DSSSD-CsI charge sharing: Tr2-1121[a]								
Track no	N_{3A}	N_{2B}	N_{2F}	N_{1S}	E_{3A} (ch)	ΔE_{2B} (MeV)	ΔE_{2F} (MeV)	ΔE_{1S} (MeV)
1	3	10	**12**	10	1908	23.9	**7.9**	5.6
2	3	10	**13**	10	1908	23.9	**15.9**	5.6
DSSSD-CsI no charge sharing: Tr2-1121[b]								
Track no	N_{3A}	N_{2B}	N_{2F}	N_{1S}	E_{3A} (ch)	ΔE_{2B} (MeV)	ΔE_{2F} (MeV)	ΔE_{1S} (MeV)
1	1	13	**6**	13	1563	5.7	**5.8**	1.4
2	1	13	**11**	13	1563	5.7	**27.2**	1.4
DSSSD-CsI multi-hit: Tr2-2121[a]								
Track no	N_{3A}	N_{2B}	N_{2F}	N_{1S}	E_{3A} (ch)	ΔE_{2B} (MeV)	ΔE_{2F} (MeV)	ΔE_{1S} (MeV)
1	**6**	5	**15**	5	**239**	18.9	**10**	4.1
2	**7**	5	**10**	5	**1023**	18.9	**8.7**	4.1
DSSSD-CsI no multi-hit: Tr2-2121[b]								
Track no	N_{3A}	N_{2B}	N_{2F}	N_{1S}	E_{3A} (ch)	ΔE_{2B} (MeV)	ΔE_{2F} (MeV)	ΔE_{1S} (MeV)
1	**3**	6	**13**	6	**3449**	10.5	**10.4**	1
2	**5**	6	**3**	6	**128**	10.5	**0.7**	1
DSSSD-CsI multi-hit: Tr4-2222								
Track no	N_{3A}	N_{2B}	N_{2F}	N_{1S}	E_{3A} (ch)	ΔE_{2B} (MeV)	ΔE_{2F} (MeV)	ΔE_{1S} (MeV)
1	0	11	12	11	3300	40.1	17.9	7.4
2	**0**	**13**	**12**	**13**	**3300**	**18**	**17.9**	**4.3**
3	**1**	**11**	**8**	**11**	**483**	**40.1**	**39.9**	**7.4**
4	1	13	8	13	483	18	39.9	4.3

momentum spectra for ^{4}He− ^{4}He and ^{2}H− ^{4}He pairs reveal distinct nuclear decay signatures. Panel (a) shows two prominent peaks around 20 MeV/c and 50 MeV/c, respectively, which correspond to the decay of the unbound ground state of ^{8}Be and the excited state of 2.43 MeV of ^{9}Be. In panel (b), the decay of the excited state of 2.186 MeV of ^{6} Li is identified by a Lorentzian fit centered at 41.38 MeV/c, which exhibits excellent agreement with the theoretical value of 42.159 MeV/c (relative deviation: 1.85%). In addition, the measurements of the energy spectra for ^{1}H, ^{2}H, and ^{3}H are presented in Fig. 15, which further validates the resolution capabilities of the detection system.

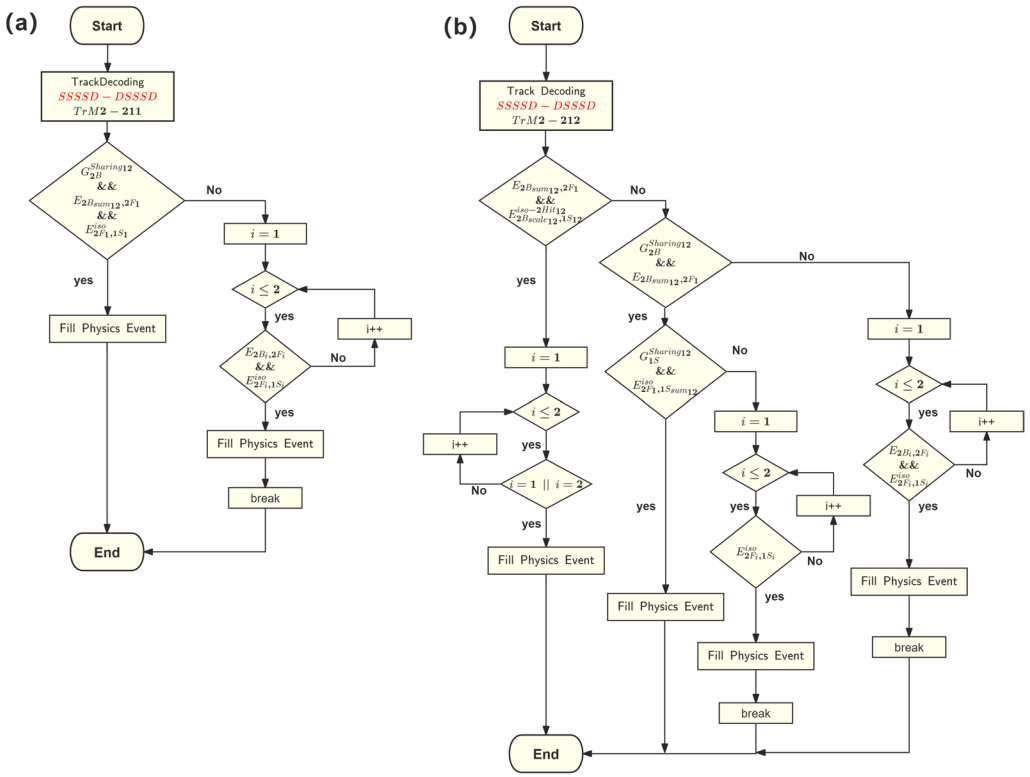

Fig. 12 (Color online) Schematic flowchart of the track decoding process for modes TrM2-211 (panel **a**) and TrM2-212 (panel **b**) in the L1L2 track reconstruction

Figure 16 illustrates the phase-space distribution of LCPs with $Z \leq 2$ for the CSHINE SSDTs in the experiment. Here, the geometric efficiency arising from the incomplete azimuthal coverage was not corrected. Rapidity, transverse momentum, and mass of the particles are denoted by y, p_t, and m_0. The curves represent the results for p_t/m_0 as functions of θ and y:

$$\frac{p_t}{m_0} = \frac{\tanh y \cdot \tan\theta}{\sqrt{1-(\tanh y/\cos\theta)^2}} \tag{8}$$

The results indicate that the CSHINE SSDTs can effectively measure LCPs over a wide θ angle range from 30° to 105° in the laboratory. This capability opens up opportunities for future physical studies, such as constraining the nuclear equation of state and investigating the isospin chronology in heavy-ion reactions at Fermi energies.

5 summary

This study introduces a comprehensive ROOT-based framework specifically developed for CSHINE-SSDTs, integrating advanced detector calibration and track reconstruction methodologies. The silicon strip detectors were precisely calibrated through systematic pulse analysis and radioactive α source measurements, while the CsI(Tl) scintillation crystals were calibrated using the ΔE_2-E_{CsI} relationship after accurate PID. The implemented track reconstruction algorithm integrates the geometric and energy constraints, effectively addressing charge-sharing phenomena and multi-hit ambiguities. After introducing reconstruction information such as the final effective identification event number and the energy spectra to optimize the detector signal threshold, the track recognition efficiencies for all SSDTs reached levels approaching or

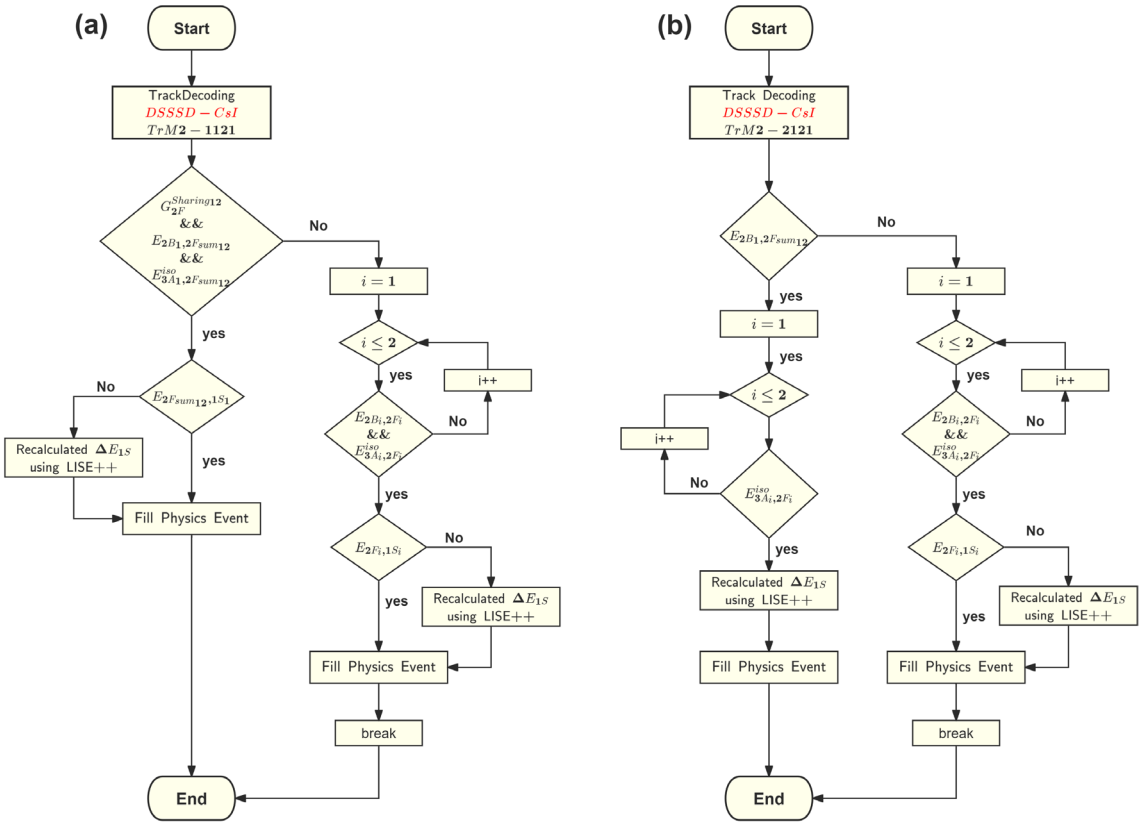

Fig. 13 (Color online) Schematic flowchart of the track decoding process for modes TrM2-1121 (panel **a**) and TrM2-2121 (panel **b**) in L2L3 track reconstruction

Table 7 Track recognition efficiencies for SSSSD-DSSSD and DSSSD-CsI

Detector	Decoding efficiency (%)	
	SSSSD-DSSSD	DSSSD-CsI
SSDT1	88.32	89.88
SSDT2	93.28	94.02
SSDT3	93.89	91.92
SSDT4	95.25	94.72

exceeding 90%. Consequently, the detection capabilities of the system were significantly enhanced. The accuracy of the detector energy calibration was evaluated by examining the characteristic peaks in the relative momentum distributions of both ^{4}He− ^{4}He and ^{2}H− ^{4}He particle pairs. The energy spectra of the hydrogen isotopes and the phase-space distribution of LCPs with $Z \leq 2$ in the 25 MeV/u ^{86}Kr + ^{124}Sn reaction were obtained. The established framework provides a robust methodology for data

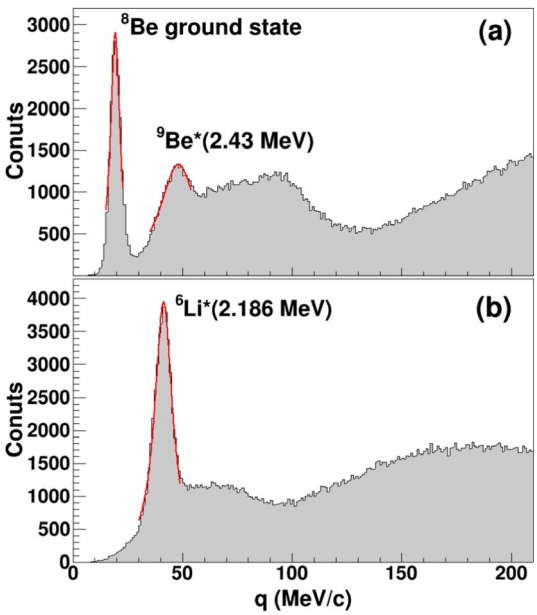

Fig. 14 (Color online) The relative momentum distributions of ^{4}He− ^{4}He and ^{2}H− ^{4}He are shown in the panels **a** and **b**, respectively

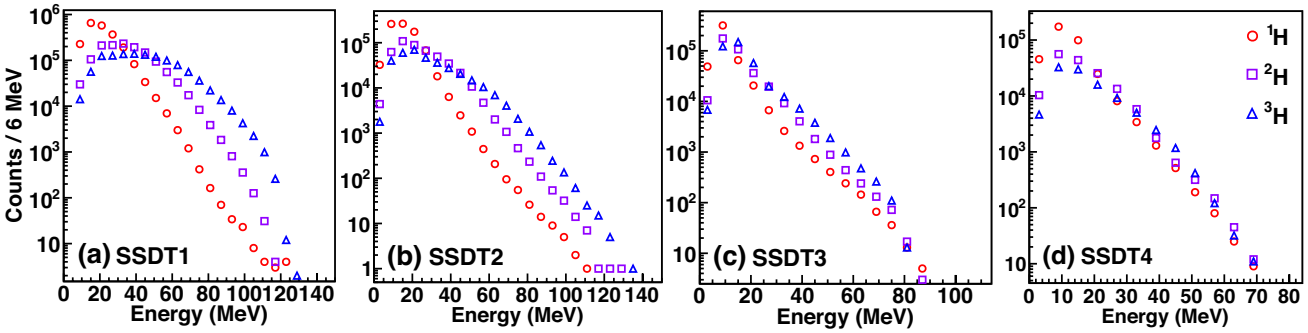

Fig. 15 (Color online) The energy spectra of hydrogen isotopes in four telescopes are displayed in panels from **a** to **d**. The open circle, square, and triangle symbols represent ^{1}H, ^{2}H, and ^{3}H, respectively

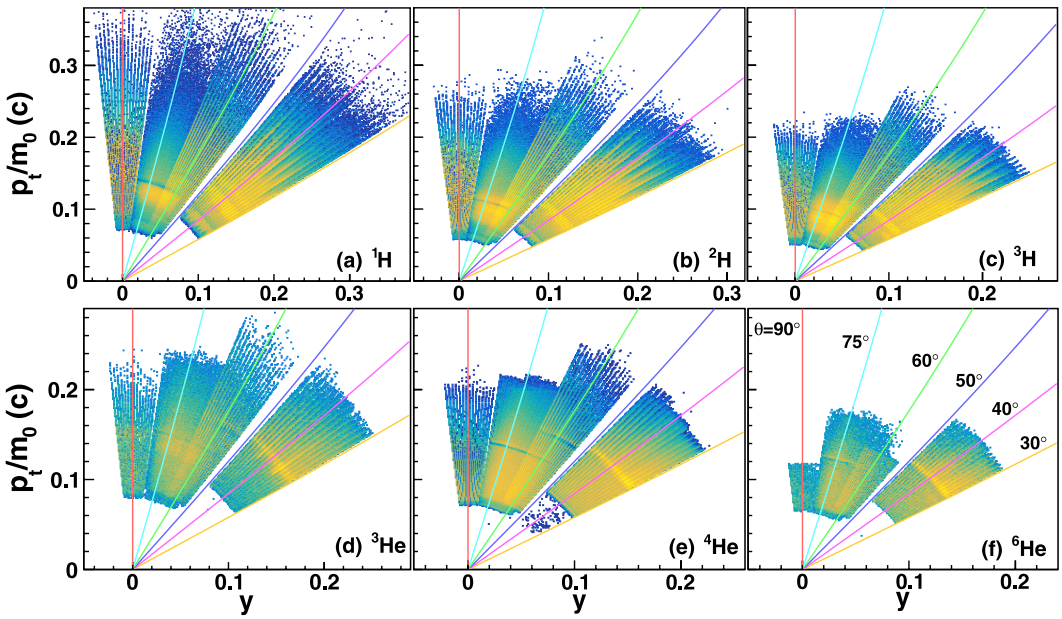

Fig. 16 (Color online) Phase space distribution of the LCPs measured by the CSHINE SSDTs in the ^{86}Kr + ^{124}Sn reactions at 25 MeV/u. From **a** to **f** shows the results of ^{1}H, ^{2}H, ^{3}H, ^{3}He, ^{4}He and ^{6}He, respectively

analysis in similar silicon telescope detector systems and offers significant potential for systematic studies in nuclear reaction experiments.

Appendix

Tables 8 and 9.

Table 8 Modes included in track reconstruction for SSSSD-DSSSD of SSDT2

L1L2	Ratio	Track reconstruction	
M	(%)	Modes	Ratio (%)
$M = 1$	77.27	Tr1-0111	100
		Tr2-0112	4.67
		Tr2-0121	46.22
$M = 2$	13.96	Tr2-0211	46.40
		Tr2-0212	2.71
		Tr3-0113	0.37
		Tr3-0131	46.00
		Tr3-0212	10.64
		Tr3-0213	2.77
$M = 3$	0.27	Tr3-0311	16.24
		Tr3-0312	23.80
		Tr3-0313	0.18
		Tr4-0122	2.45
		Tr4-0212	3.21
$M = 4$	5.74	Tr4-0141	0.06
		Tr4-0221	17.81
		Tr4-0222	76.25
Total	97.24	-	-

Table 9 Modes included in track reconstruction for DSSSD-CsI of SSDT2

L2L3	Ratio	Track reconstruction	
M	(%)	Modes	Ratio (%)
M=1	79.98	Tr1-1111	100
		Tr2-1112	3.69
		Tr2-1121	50.31
		Tr2-1211	21.78
		Tr2-1212	10.70
M=2	13.56	Tr2-2111	2.79
		Tr2-2121	2.17
		Tr2-2212	0.91
		Tr2-2222	7.64
		Tr3-1113	0.06
		Tr3-1131	17.12
		Tr3-1212	17.25
		Tr3-1213	1.67
		Tr3-1311	1.45
		Tr3-1312	9.62
		Tr3-2121	6.49
		Tr3-2131	2.17
M=3	1.20	Tr3-2211	2.23
		Tr3-2212	1.86
		Tr3-2221	0.54
		Tr3-2222	18.80
		Tr3-2223	0.87
		Tr3-2232	7.18
		Tr3-2322	5.23
		Tr3-3222	4.03
		Tr3-3333	0.06
		Tr4-1122	4.56
		Tr4-1212	22.92
		Tr4-1221	14.29
		Tr4-1222	25.51
M=4	3.37	Tr4-2122	1.44
		Tr4-2221	2.11
		Tr4-2222	23.36
		Tr4-3333	0.01
Total	98.11	-	-

Author contributions All authors contributed to the conception and design of this study. Material preparation, coding, and analyses were performed by XBW. YJW is responsible for code review, analysis, and result checking. The first draft of the manuscript was written by XBW and modified by CWM/YJW/ZGX. The project was led and supervised by CWM/YJW/ZGX. All authors commented on previous versions of the manuscript and read and approved the final manuscript.

Data availibility The data that support the findings of this study are openly available in Science Data Bank at https://cstr.cn/31253.11.sciencedb.j00186.00708 and https://doi.org/10.57760/sciencedb.j00186.00708.

Declarations

Conflict of interest Chun-Wang Ma is an editorial board member for Nuclear Science and Techniques and was not involved in the editorial review, or the decision to publish this article. All authors declare that there are no Conflict of interest.

References

1. G.Y. Cheng, Q.M. Su, X.G. Cao et al., The study of intelligent algorithm in particle identification of heavy-ion collisions at low and intermediate energies. Nucl. Sci. Tech. **35**, 33 (2024). https://doi.org/10.1007/s41365-024-01388-3
2. F.H. Guan, X.Y. Diao, Y.J. Wang et al., A compact spectrometer for heavy ion experiments in the fermi energy regime. Nucl. Instrum. Meth. A **1011**, 165592 (2021). https://doi.org/10.1016/j.nima.2021.165592
3. D. Guo, Y.H. Qin, S. Xiao et al., An FPGA-based trigger system for CSHINE. Nucl. Sci. Tech. **33**, 162 (2022). https://doi.org/10.1007/s41365-022-01149-0
4. Z. Sun, W.L. Zhan, Z.Y. Guo et al., RIBLL, the radioactive ion beam line in Lanzhou. Nucl. Instrum. Meth. A **503**, 496 (2003). https://doi.org/10.1016/S0168-9002(03)01005-2
5. X.H. Zhou, The heavy ion research facility in Lanzhou. Nucl. Phys. News **26**, 4 (2016). https://doi.org/10.1080/10619127.2016.1177330
6. F.H. Guan, Y.J. Wang, X.Y. Diao et al., Track recognition for the telescopes with silicon strip detectors. Nucl. Instrum. Meth. A **1029**, 166461 (2022). https://doi.org/10.1016/j.nima.2022.166461
7. Y.J. Wang, F.H. Guan, X.Y. Diao et al., CSHINE for studies of HBT correlation in heavy ion reactions. Nucl. Sci. Tech. **32**, 4 (2021). https://doi.org/10.1007/s41365-020-00842-2
8. Y.J. Wang, F.H. Guan, Q.H. Wu et al., The emission order of hydrogen isotopes via correlation functions in 30 MeV/u Ar + Au reactions. Phys. Lett. B **825**, 136856 (2022). https://doi.org/10.1016/j.physletb.2021.136856
9. Y. Zhang, J.L. Tian, W.J. Cheng et al., Long-time drift of the isospin degree of freedom in heavy ion collisions. Phys. Rev. C **95**, 041602 (2017). https://doi.org/10.1103/PhysRevC.95.041602
10. Y.J. Wang, F.H. Guan, X.Y. Diao et al., Observing the ping-pong modality of the isospin degree of freedom in cluster emission from heavy-ion reactions. Phys. Rev. C **107**, L041601 (2023). https://doi.org/10.1103/PhysRevC.107.L041601
11. X.Y. Diao, F.H. Guan, Y.J. Wang et al., Reconstruction of fission events in heavy ion reactions with the compact spectrometer for heavy ion experiment. Nucl. Sci. Tech. **33**, 40 (2022). https://doi.org/10.1007/s41365-022-01024-y
12. L. Li, F.Y. Wang, Y.X. Zhang et al., Isospin efects on intermediate mass fragments at intermediate energy-heavy ion collisions. Nucl. Sci. Tech. **33**, 58 (2022). https://doi.org/10.1007/s41365-022-01050-w
13. Q.H. Wu, F.H. Guan, X.Y. Diao et al., Symmetry energy effect on emissions of light particles in coincidence with fast fission. Phys. Lett. B **811**, 132565 (2020). https://doi.org/10.1016/j.physletb.2020.135865
14. Q.H. Wu, X.Y. Diao, F.H. Guan et al., Transport model studies on the fast fission of the target-like fragments in heavy ion collisions. Phys. Lett. B **797**, 134808 (2019). https://doi.org/10.1016/j.physletb.2019.134808
15. Y.H. Qin, D. Guo, S. Xiao et al., A CsI(Tl) hodoscope on CSHINE for Bremsstrahlung γ-rays in heavy ion reactions. Nucl. Instrum. Meth. A **1053**, 168330 (2022). https://doi.org/10.1016/j.nima.2023.168330
16. Y.H. Qin, Q.L. Niu, D. Guo et al., Probing high-momentum component in nucleon momentum distribution by neutron-proton bremsstrahlung γ-rays in heavy ion reactions. Phys. Lett. B **850**, 138514 (2024). https://doi.org/10.1016/j.physletb.2024.138514
17. Z.L. Liao, X.G. Cao, Y.X. Yang et al., Design and construction of charged-particle telescope array for study of exotic nuclear clustering structure. Nucl. Sci. Tech. **35**, 134 (2024). https://doi.org/10.1007/s41365-024-01503-4
18. H.Y. Zhu, J.L. Lou, Y.L. Ye et al., Two annular CsI(Tl) detector arrays for the charged particle telescopes. Nucl. Sci. Tech. **34**, 159 (2023). https://doi.org/10.1007/s41365-023-01319-8
19. O. Tarasov, Analysis of momentum distributions of projectile fragmentation products. Nucl. Phys. A **734**, 536 (2004). https://doi.org/10.1016/j.nuclphysa.2004.01.099
20. G. Cardella, N.S. Martorana, L. Acosta et al., Pixelation method for the FARCOS array. Nucl. Instrum. Meth. A **1069**, 169961 (2024). https://doi.org/10.1016/j.nima.2024.169961
21. https://gitee.com/DB-weixiaobao/ana-framework
22. N. Le Neindre, M. Alderighi, A. Anzalone et al., Mass and charge identification of fragments detected with the Chimera Silicon-CsI(Tl) telescopes. Nucl. Instrum. Meth. A **490**, 251 (2002). https://doi.org/10.1016/S0168-9002(02)01008-2
23. L. Tassan-Got, A new functional for charge and mass identification in $\Delta E - E$ telescopes. Nucl. Instrum. Meth. B **194**, 503 (2002). https://doi.org/10.1016/S0168-583X(02)00957-6
24. W. Gawlikowicz, J. Tõke, W.U. Schröder, A calibration method for phoswich detectors. Nucl. Instrum. Meth. A **491**, 181 (2002). https://doi.org/10.1016/S0168-9002(02)01230-5
25. B. Davin, R.T. de Souza, R. Yanez et al., LASSA: a large area silicon strip array for isotopic identification of charged particles. Nucl. Instrum. Meth. A **473**, 302 (2001). https://doi.org/10.1016/S0168-9002(01)00295-9
26. Q. Liu, Y.L. Ye, Z.H. Li et al., Investigation of the thickness non-uniformity of the very thin silicon-strip detectors. Nucl. Instrum. Meth. A **897**, 100 (2018). https://doi.org/10.1016/j.nima.2018.04.041
27. J.F. Ziegler, J.P. Biersack, *The stopping and range of ions in matter* (Pergamon Press, New York, 1985)
28. D. Dell'Aquila, S. Sweany, K.W. Brown et al., Non-linearity effects on the light-output calibration of light charged particles in CsI(Tl) scintillator crystals. Nucl. Instrum. Meth. A **929**, 162 (2019). https://doi.org/10.1016/j.nima.2019.03.065
29. D. Horn, G.C. Ball, A. Galindo-Uribarri et al., The mass dependence of CsI(Tl) scintillation response to heavy ions. Nucl. Instrum. Meth. A **320**, 273 (1992). https://doi.org/10.1016/0168-9002(92)90785-3
30. J.H. Chen, X. Dong, X.H. He et al., Properties of the QCD matter: review of selected results from the relativistic heavy ion collider beam energy scan (RHIC BES) program. Nucl. Sci. Tech. **35**, 214 (2024). https://doi.org/10.1007/s41365-024-01591-2